

# Electron-phonon coupling and pairing mechanism in $\beta$ -Bi<sub>2</sub>Pd centrosymmetric superconductor

Jing-Jing Zheng<sup>1,2</sup> and E. R. Margine<sup>1,\*</sup>

<sup>1</sup>*Department of Physics, Applied Physics and Astronomy,  
Binghamton University-SUNY, Binghamton, New York 13902, USA*

<sup>2</sup>*Institute of Theoretical Physics and Department of Physics,  
Shanxi University, Taiyuan 030006, People's Republic of China*

We report first-principles calculations of the superconducting properties of  $\beta$ -Bi<sub>2</sub>Pd within the fully anisotropic Migdal-Eliashberg formalism. We find a single anisotropic superconducting gap of  $s$ -wave symmetry which varies in magnitude on the different regions of the Fermi surface. The calculated superconducting energy gap on the Fermi surface, the superconducting transition temperature, the specific heat, and the quasi-particle density of states are in good agreement with the corresponding experimental results and support the view that  $\beta$ -Bi<sub>2</sub>Pd is a phonon-mediated single anisotropic gap superconductor.

## INTRODUCTION

In recent years considerable attention has been devoted to the study of superconductors in the Bi-Pd family of alloys [1–4], in particular, the non-centrosymmetric  $\alpha$ -BiPd [5–8] and the centrosymmetric  $\beta$ -Bi<sub>2</sub>Pd [9–17] compounds that have been found to exhibit topologically protected surface states with Rashba-like spin splitting. While the superconducting state of  $\alpha$ -BiPd appears to be topologically trivial [6, 7], the structure of the superconducting gap and the role of the topologically protected surface states in the superconducting pairing mechanism of  $\beta$ -Bi<sub>2</sub>Pd still remain to be clarified. An early experimental study has suggested that  $\beta$ -Bi<sub>2</sub>Pd is a multi-gap/multiband superconductor based on the temperature dependence of the electronic specific heat and the upper critical magnetic field data [9]. In contrast, recent scanning tunneling microscopy, calorimetric, Hall-probe magnetometry, muon spin relaxation, and point-contact spectroscopy measurements point towards a single  $s$ -wave superconducting gap [10–13]. Finally, while the absence of topological Andreev bound states in point-contact data [13] excludes the possibility of a topological superconducting behavior at the surface of  $\beta$ -Bi<sub>2</sub>Pd, Majorana zero modes have been identified in  $\beta$ -Bi<sub>2</sub>Pd crystalline films [14].

In this work, we present the first theoretical study of the phonons and the role of the electron-phonon interaction in the superconducting state of  $\beta$ -Bi<sub>2</sub>Pd by performing state-of-the-art *ab initio* calculations powered by electron-phonon Wannier interpolation [18–20]. Since the strong spin-orbit coupling (SOC) inherent to the heavy element Bi induces significant changes in the electronic band structure [15, 16],  $\beta$ -Bi<sub>2</sub>Pd compound offers the opportunity to further study the interplay of the spin-orbit coupling effect with superconductivity. We find that  $\beta$ -Bi<sub>2</sub>Pd displays BCS-like superconductivity with a single anisotropic superconducting gap in agreement with recent experimental findings [10–13].

## METHODOLOGY

The calculations are performed within the generalized gradient approximation to density-functional theory [21], employing fully relativistic norm-conserving pseudopotentials [22, 23], as implemented in the Quantum-ESPRESSO suite [24]. The Perdew, Burke, and Ernzerhof (PBE) [25] form of the generalized gradient approximation was chosen to describe the exchange-correlation energy. The planewaves kinetic energy cutoff is 40 Ry. The Bi  $6s^2 6p^3$  and the Pd  $4d^9 5s^1$  orbitals were included as valence electrons. The  $\beta$ -Bi<sub>2</sub>Pd phase crystallizes in the centrosymmetric body-centered tetragonal crystal structure with space group  $I4/mmm$  (No.139). To facilitate the comparison with the experimental results, we employ the experimental lattice constants ( $a = 3.362$  Å and  $c = 12.983$  Å [1]) for calculations without and with SOC [26]. A similar approach has been used in previous studies of superconductivity and charge density wave instability of other layered materials [27–30]. In both cases, the atomic positions were relaxed using a threshold of 10 meV/Å for the forces. The optimized internal parameter  $z_{Bi}$  for Bi atom is 0.361 (without SOC) and 0.362 (with SOC), which are in good agreement with the experimentally reported value of  $z_{Bi} = 0.363$  [1]. The electronic charge density is calculated using an unshifted Brillouin zone (BZ) mesh with  $12^3$   $\mathbf{k}$ -points and a Methfessel-Paxton smearing of 0.02 Ry. The dynamical matrices and the linear variation of the self-consistent potential are calculated within density-functional perturbation theory [31] on the irreducible set of a regular  $4^3$   $\mathbf{q}$ -point mesh.

The superconducting gap is evaluated using the anisotropic Migdal-Eliashberg formalism [32, 33] as implemented in the EPW code [33–35]. We have recently used this methodology to investigate the superconducting properties of layered and two-dimensional materials with highly anisotropic Fermi surfaces [36–39]. The electronic wavefunctions required for the Wannier-Fourier in-

terpolation [18, 40] in EPW are calculated on a uniform unshifted Brillouin-zone grids of size  $8^3$ . Eleven maximally localized Wannier functions, three  $p$  states for each Bi atom and five  $d$  states for Pd atom, are included to describe the electronic structure near the Fermi level. For the anisotropic Migdal-Eliashberg equations we use  $90^3$   $\mathbf{k}$ -point and  $45^3$   $\mathbf{q}$ -point grids. The Matsubara frequency cutoff is set to 7.5 times the largest phonon frequency, and the Dirac delta functions are replaced by Lorentzians of widths 25 meV and 0.05 meV for electrons and phonons, respectively.

The technical details of the Migdal-Eliashberg calculations have been described extensively in Refs. [33] and [35], here we only outline briefly the main procedure. In order to calculate the superconducting properties the fully anisotropic Migdal-Eliashberg equations are solved self-consistently along the imaginary axis at the fermion Matsubara frequencies  $\omega_n = (2n+1)\pi T$  (with  $n$  an integer) for each temperature  $T$ :

$$Z(\mathbf{k}, i\omega_n) = 1 + \frac{\pi T}{N_F \omega_n} \sum_{\mathbf{k}' n'} \frac{\omega_{n'}}{\sqrt{\omega_{n'}^2 + \Delta^2(\mathbf{k}', i\omega_{n'})}} \times \delta(\epsilon_{\mathbf{k}'}) \lambda(\mathbf{k}, \mathbf{k}', n - n'), \quad (1)$$

$$Z(\mathbf{k}, i\omega_n) \Delta(\mathbf{k}, i\omega_n) = \frac{\pi T}{N_F} \sum_{\mathbf{k}' n'} \frac{\Delta(\mathbf{k}', i\omega_{n'})}{\sqrt{\omega_{n'}^2 + \Delta^2(\mathbf{k}', i\omega_{n'})}} \times \delta(\epsilon_{\mathbf{k}'}) [\lambda(\mathbf{k}, \mathbf{k}', n - n') - \mu^*]. \quad (2)$$

$Z(\mathbf{k}, i\omega_n)$  is the mass renormalization function,  $\Delta(\mathbf{k}, i\omega_n)$  is the superconducting gap function,  $\lambda(\mathbf{k}, \mathbf{k}', n - n')$  is the momentum- and energy-dependent electron-phonon coupling,  $\mathbf{k}$  ( $\mathbf{k}'$ ) is an electronic state of combined band and momentum index, and  $\mu^*$  is the semiempirical Coulomb parameter [41]. The anisotropic  $\lambda(\mathbf{k}, \mathbf{k}', n - n')$  to be used in the Migdal-Eliashberg equations is given by:

$$\lambda(\mathbf{k}, \mathbf{k}', n - n') = N_F \sum_{\nu} \frac{2\omega_{\mathbf{q}\nu}}{(\omega_n - \omega_{n'})^2 + \omega_{\mathbf{q}\nu}^2} |g_{\mathbf{k}\mathbf{k}'}^{\nu}|^2. \quad (3)$$

From the superconducting gap function  $\Delta(\mathbf{k}, i\omega_n)$  one obtains the superconducting gap at real-valued frequencies  $\Delta(\mathbf{k}, \omega)$  via Padé approximants [44, 45]. The superconducting critical temperature  $T_c$  is identified as the temperature at which the leading edge  $\Delta(\mathbf{k}, \omega = 0)$  of the superconducting gap vanishes.

## ELECTRONIC AND VIBRATIONAL PROPERTIES

Figures 1(a) and (b) depict the decomposed band structure of  $\beta$ -Bi<sub>2</sub>Pd along the main high-symmetry directions of the Brillouin zone [46] calculated without and with the inclusion of spin-orbit coupling. As previously reported [15, 16], four bands of mixed orbital character

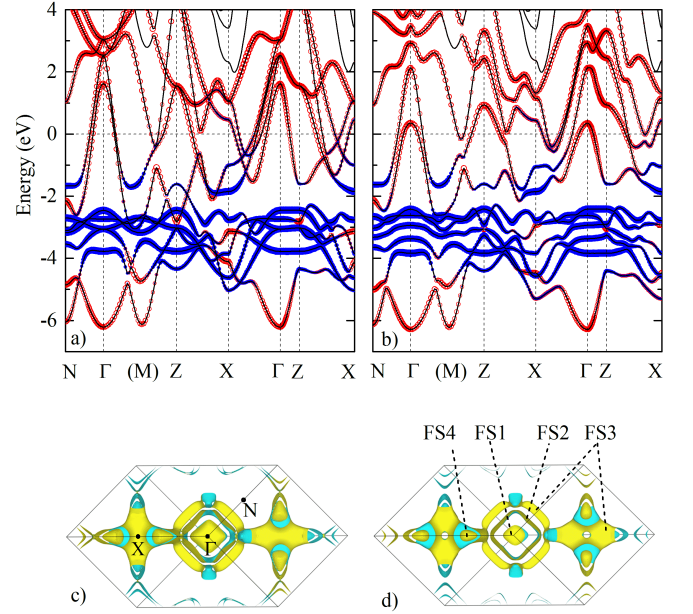


FIG. 1: (Color online) Electronic band structure of bulk  $\beta$ -Bi<sub>2</sub>Pd (a) without SOC and (b) with SOC. The size of the blue and red symbols is proportional to the contribution of Pd- $d$  and Bi- $p$  character. The corresponding Fermi surfaces are plotted in (c) and (d). The inner surface is shown in cyan, while the outer part in yellow. The connection between the reciprocal lattice and the BZ is shown in Supplemental Fig. S1 [47]. The hole pockets are labeled as FS1 and FS2 and the electron pockets are labeled as FS3 and FS4.

cross the Fermi level. The two hole-like bands centered around the  $\Gamma$  point originate from the Bi- $6p_{x+y}/p_z$  orbitals, while the two electron-like bands along the  $\Gamma$ -X direction originate from the Bi- $6p_{x+y}/p_z$  and Pd- $4d_{xz+yz}/d_{xy}$  orbitals. These bands give rise to a complex multiple sheet Fermi surface (FS) topology [16] that has been recently resolved using angular-resolved photoemission spectroscopy [15]. As shown in Figs. 1(c)-(d), the Fermi surface consists of a deformed two-dimensional cylindrical hole-like sheet (FS2) enclosing a smaller hole pocket (FS1) centered around the  $\Gamma$  point. Surrounding the surface of the outer hole pocket, there is a three-dimensional electron pocket (FS3) which confines a second smaller electron pocket (FS4) along the  $\Gamma$ -X direction.

The inclusion of the SOC leads to the splitting of bands around the Fermi level and the opening of two continuous gaps that extend over the whole Brillouin zone as shown in Fig. 1(b). As a result, the electronic density of states at the Fermi level ( $N_F$ ) is increased by approximately 20%, from 0.659 to 0.788 states/spin/(eV unit cell). Finally, there is a noticeable reduction in the size of the  $\Gamma$ -centered hole and electron pockets, although the Fermi surface topology remains unchanged with the inclusion of SOC.

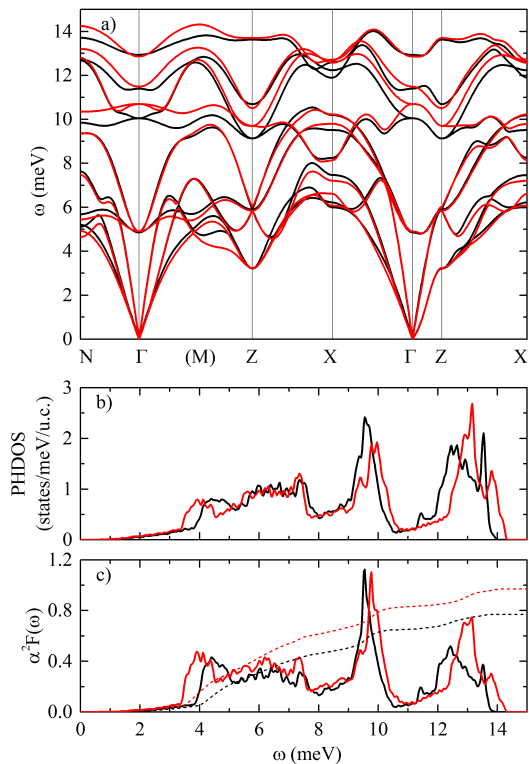


FIG. 2: (Color online) (a) Phonon dispersion relations and (b) phonon density of states of  $\beta$ -Bi<sub>2</sub>Pd. (c) Isotropic Eliashberg spectral function  $\alpha^2 F(\omega)$  (solid line) and cumulative electron-phonon coupling strength  $\lambda(\omega)$  (dashed line). The data without and with SOC are presented in black and red, respectively.

In Figs. 2(a) and (b), we compare the phonon dispersion relations and the phonon density of states (PHDOS) calculated without and with SOC. In both cases, three regions can be clearly distinguished in the PHDOS: a low-energy region that extends up to 8.0 meV, an intermediate region from 8.0 to 10.0 meV, and a high-energy region above 10.0 meV. The decomposition of the phonon spectrum with respect to atomic vibrations is provided in Supplemental Fig. S2 [47]. The three acoustic phonon branches have a mixed character with both types of atoms involved in the lattice vibration. That also holds for the first two optical branches. The higher optical phonons stem mostly from the vibration of Pd atoms, consistent with their lighter mass. The phonon spectrum only changes slightly with the inclusion of SOC. The frequencies of the highest optical modes are pushed upward by about 0.36 meV (2.5 %) across the whole BZ, while the lowest acoustic branch softens along the  $\Gamma$ -Z direction.

In order to quantify the interaction between electrons and phonons, we calculate the Eliashberg spectral function,  $\alpha^2 F(\omega)$ , and the cumulative electron-phonon coupling (EPC) strength,  $\lambda(\omega)$ . As shown in Fig. 2(c), the Eliashberg spectral function follows the trend of the PH-

DOS and exhibits a similar peak structure. Although the phonons from all energy regions contribute to the total EPC, the relative contributions of each set of modes differ considerably. The low-energy modes (up to 8.0 meV) account for approximately 60% of the total coupling ( $\lambda = 0.77$ ), while the phonons in the intermediate- and high-energy regions have a less sizable contribution of 22% and 18%, respectively. With inclusion of SOC,  $\lambda$  increases by 26% to 0.97. The SOC-induced enhancement of  $\lambda$  correlates with the increased density of states at the Fermi level and the softening of the low-energy phonon modes. In particular, the phonons in the low-energy region account for 0.15 of the total increase in  $\lambda$ , while the phonons in the intermediate- and high-energy regions only account for 0.01 and 0.04, respectively.

### SUPERCONDUCTING PROPERTIES

After assessing the EPC, we investigate its effect on the superconducting pairing mechanism. The superconducting gap function and the critical temperature are estimated by solving the anisotropic Migdal-Eliashberg equations [32, 33, 35]. Figs. 3(a)–(b) show the energy distribution of the superconducting gap at the Fermi level as a function of temperature calculated without and with SOC and for a typical Coulomb pseudopotential  $\mu^* = 0.1$ . We find that  $\beta$ -Bi<sub>2</sub>Pd exhibits an anisotropic single-gap structure characterized by a relatively broad energy profile with a spread of 0.38 meV (without SOC) and 0.34 meV (with SOC). The average value of the gap at zero temperature is estimated to be  $\Delta(0) = 0.65$  meV (without SOC) and  $\Delta(0) = 0.70$  meV (with SOC). These values are in good agreement with scanning tunneling microscopy and muon spin relaxation measurements yielding 0.76 meV [10] and 0.78 meV [12], respectively. Slightly larger values of 0.88 meV and 0.92 meV were reported based on calorimetric and Hall-probe magnetometry measurements [11, 48], in the first case, and point-contact spectroscopy measurements [13], in the second case. It is noteworthy that scanning tunneling measurements performed on the same samples as used for the calorimetric and Hall-probe magnetometry measurements returned a superconducting gap in the 0.77–0.82 meV range [11, 49]. These differences in the experimental results still remain to be understood, with one possible cause the surface proximity effect [11]. Based on the Migdal-Eliashberg results, the superconducting gap vanishes at a critical temperature  $T_c = 4.40$  K (without SOC) and  $T_c = 4.55$  K (with SOC), close to the lower limit of the reported experimental values ranging from 4.25 K to 5.4 K [1, 2, 9–13, 15]. In order to test the sensitivity of our results to the parameters entering in the Migdal-Eliashberg equations, we have repeated the calculations for different electron and phonon meshes, smearing values, and Matsubara frequency cutoffs. The super-

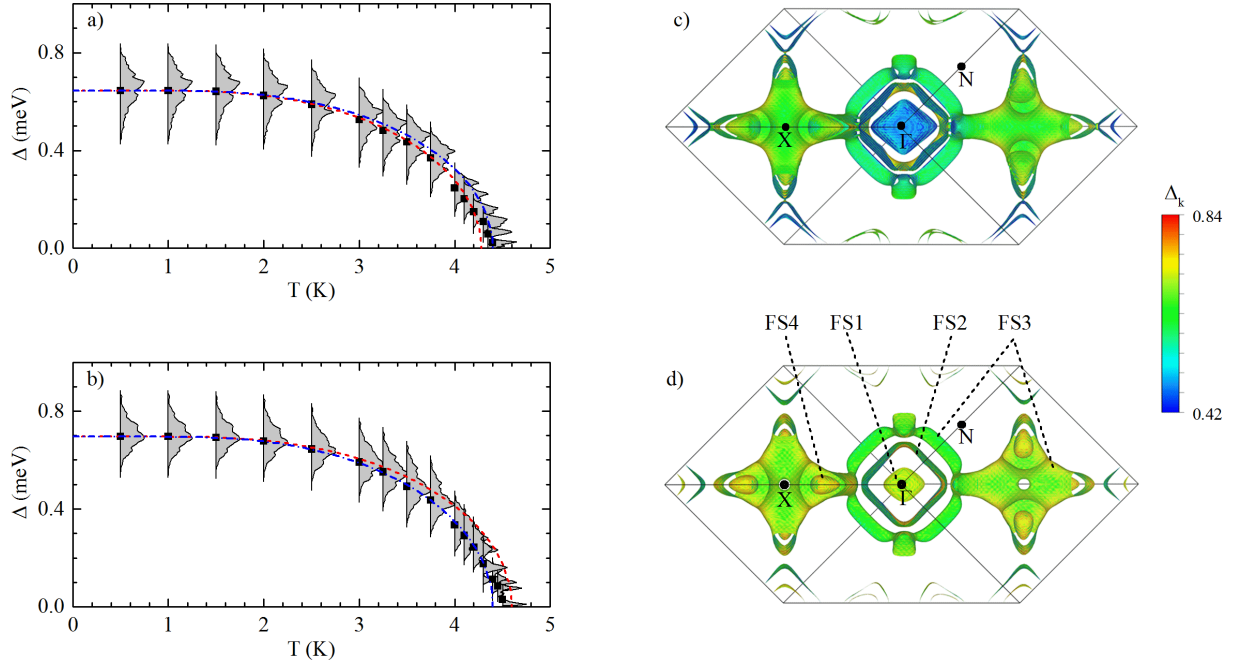


FIG. 3: (Color online) Energy distribution of the anisotropic superconducting gap  $\Delta_{\mathbf{k}}$  of  $\beta$ -Bi<sub>2</sub>Pd as a function of temperature (a) without SOC and (b) with SOC. The gap is calculated using a Coulomb pseudopotential  $\mu^*$  of 0.1. The black squares represent the average value of the gap which vanishes at the critical temperature  $T_c = 4.40$  K (without SOC) and 4.55 K (with SOC). The red dashed and blue dashed dotted lines are fits to the calculated data based on the BCS model and  $\alpha$  model, respectively. Momentum-resolved superconducting gap  $\Delta_{\mathbf{k}}$  (in meV) on the Fermi surface of  $\beta$ -Bi<sub>2</sub>Pd at 1 K (c) without SOC and (d) with SOC.

conducting gap and critical temperature are found to be converged within 5%.

Figures 3 (c) and (d) show the superconducting gap at 1 K on different parts of the Fermi surface. The same figures under three different perspectives are shown in Supplemental Fig. S3 [47]. We can clearly see that the gap opens on both the electron and hole pockets, and the magnitude of the gap changes greatly on some of the Fermi surface sheets. An essentially isotropic distribution is observed on the Bi-dominated inner hole FS1 pocket and the central region of the three-dimensional electron FS3 sheet with mixed Bi and Pd orbital character. On the contrary, the other parts of the Fermi surface display a strong anisotropy, in particular, the nearly cylindrical FS2 sheet shows the largest spread in  $\Delta_{\mathbf{k}}$ . Although the topology of the superconducting gap on the Fermi surface is practically not modified by the inclusion of the SOC, there is a noticeable difference between the absolute value of the gap on the inner Fermi surface. In the latter case, the superconducting gap is no longer characterized by a small spread around the minimum value, but around the average value of  $\Delta_{\mathbf{k}}$ . This change is likely driven by the softening of the lowest acoustic branch along the  $\Gamma$ -Z direction which involves mainly out-plane Bi<sub>z</sub> phonons. The structure of the gap correlates closely with the variation of the electron-phonon coupling strength on the

individual Fermi surface sheets shown in Supplemental Fig. S4 [47].

We further fit the temperature dependence of the average value of the superconducting gap using the single-band BCS *s*-wave model [50] and the single-band  $\alpha$  model [51]. In the first case, we obtain the temperature-dependent gap by solving numerically the BCS gap equation [50, 52]

$$\int_0^{\frac{k_B \theta_D}{\Delta(0)}} \tanh\left(\frac{\alpha_{BCS} \tilde{E}}{2t}\right) \frac{d\tilde{E}}{\tilde{E}} = \ln\left[\frac{2k_B \theta_D}{\Delta(0)}\right], \quad (4)$$

with  $\Delta(0)$  taken from our first-principles calculations. Here  $\alpha_{BCS} = 1.764$ ,  $t = T/T_c$  is the reduced temperature,  $\tilde{\varepsilon} = \varepsilon/\Delta(0)$  is the normalized normal-state single-particle energy,  $k_B \theta_D$  is the maximum phonon energy within the Debye theory set to 1000,  $\tilde{E} = \sqrt{\tilde{\varepsilon}^2 + \tilde{\Delta}^2}$  is the normalized excited quasi-particle (electron and hole) energy, and  $\tilde{\Delta} = \Delta/\Delta(0)$  is the superconducting gap normalized by its zero temperature value. In the second case, the data is fitted using the single-gap  $\alpha$  model [51, 52] which extends the BCS theory by introducing an adjustable parameter  $\alpha = \Delta(0)/k_B T_c$ . In this model the reduced gap  $\tilde{\Delta}$  is assumed to be the same as in the BCS theory calculated from Eq. (4).

The results obtained with the two models are shown in

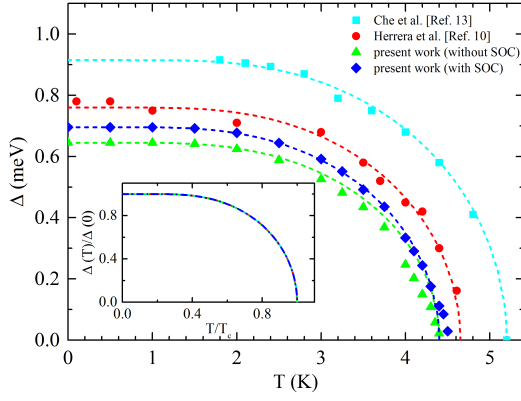


FIG. 4: (Color online) Comparison between theoretical and experimental [10, 13] superconducting gaps as a function of temperature. The theoretical data represent the average value of the gap extracted from Figs. 3(a) and (b). The curves are fits to the superconducting gap values within the  $\alpha$  model.

Figs. 3(a)–(b) as red dashed and blue dashed dotted lines. Within the  $\alpha$  model, the fitting parameters are found to be  $\alpha = 1.71$  and  $\alpha = 1.85$  for the calculations without and with SOC. All fitting curves give an overall good description of the temperature dependence of the superconducting gaps, although noticeable deviations can be seen in the region around the critical temperature. In particular, the two sets of *ab initio* data are best reproduced by the BCS model for calculations without SOC and by the  $\alpha$  model for calculations with SOC, respectively.

In Fig. 4 we compare our results for the superconducting gap with the experimental data extracted from scanning tunneling microscopy [10] and point-contact spectroscopy [13] measurements. We find that both sets of experimental gaps are best fitted with the  $\alpha$  model, similarly to our SOC calculations. We obtain  $\alpha = 1.90$  for the tunneling conductance data and  $\alpha = 2.05$  for point-contact data, respectively. For comparison, the fits obtained with the BCS model display much larger deviations as shown in Supplemental Fig. S5 [47]. The overall agreement between the theory and experiment is good, the temperature behavior of the superconducting gap (i.e., the shape of the curve) is almost perfectly reproduced. This can be more clearly seen in the inset in Fig. 4, where we plot the normalized superconducting gap  $\Delta(T)/\Delta(0)$  versus the reduced temperature  $T/T_c$ .

Next, the temperature dependence of the normalized electronic specific heat in the superconducting state is calculated within the  $\alpha$  model using the following expression [52]:

$$\frac{C_{es}(t)}{\gamma_n T_c} = \frac{6\alpha^3}{\pi^2 t} \int_0^\infty [f(1-f) \left( \frac{\tilde{E}^2}{t} - \frac{1}{2} \frac{d\tilde{\Delta}^2}{d\tilde{t}} \right)] d\tilde{\epsilon}, \quad (5)$$

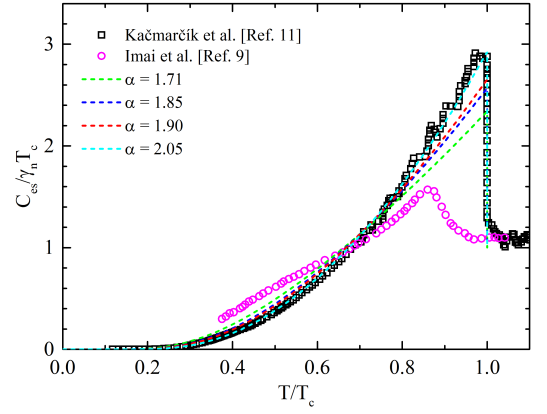


FIG. 5: (Color online) Calculated and experimental normalized electronic specific heat as a function of  $T/T_c$ .

where  $f = [\exp(\alpha \tilde{E}/t) + 1]^{-1}$  is the Fermi-Dirac distribution function and  $\gamma_n = (2/3)\pi^2 k_B^2 N_F$  is the Sommerfeld coefficient. The temperature derivative of the gap function  $d\tilde{\Delta}^2(t)/dt$  is given by [52]:

$$\frac{d\tilde{\Delta}^2(t)}{dt} = \frac{\int_0^\infty \text{sech}^2(g) d\tilde{\epsilon}}{\int_0^\infty \left[ \frac{t \text{sech}^2(g)}{2(\tilde{\epsilon}^2 + \tilde{\Delta}^2)} - \frac{t^2 \tanh(g)}{\alpha_{BCS}(\tilde{\epsilon}^2 + \tilde{\Delta}^2)^{3/2}} \right] d\tilde{\epsilon}}, \quad (6)$$

where  $g = \frac{\alpha_{BCS} \sqrt{\tilde{\epsilon}^2 + \tilde{\Delta}^2}}{2t}$ . In Fig. 5 we plot the reduced specific heat obtained from the temperature dependence of the superconducting gap corresponding to the four fits based on the  $\alpha$  model in Fig. 4 together with the experimental data extracted from thermal-relaxation [9] and calorimetric [11] measurements. To facilitate the comparison, we renormalize the temperature to  $T_c$ , using the corresponding experimental and theoretical values. The normalization procedure for the experimental data is shown in Supplemental Fig. S6 [47]. The results for  $\alpha < 2$  associated with the theoretical data (green and blue dashed lines) and scanning tunneling microscopy data (red dashed line) compare well over the whole temperature range. The discontinuity at the critical temperature  $\Delta C_e / \gamma_n T_c = 1.426(\alpha/\alpha_{BCS})^2$  is found to be 1.34 (for  $\alpha = 1.71$ ), 1.57 (for  $\alpha = 1.85$ ) and 1.65 (for  $\alpha = 1.90$ ), close to the BCS value of 1.43. A larger discrepancy is observed, particularly in the high-temperature region  $t > 0.8$ , when the results for  $\alpha < 2$  are compared to the ones for  $\alpha = 2.05$  associated with the point-contact data (cyan dashed line) and the calorimetric specific heat measurements (black squares) [11]. In the latter two cases, the jump at the critical temperature is estimated to be 1.93. Despite the aforementioned differences, all these results give a specific heat temperature dependence consistent with the one-gap BCS model. Moreover, they differ strikingly from the earlier specific heat measurements (magenta circles), disproving the sug-



gestion of multigap superconductivity [9].

The argument for a multigap scenario presented in Ref. [9] was based on the appearance of an additional hump in the specific heat at approximately 3 K as shown in Supplemental Fig. S6(a). A similar low-temperature feature observed in the  $\text{MgB}_2$  superconductor at approximately 10 K was caused by a second energy gap [53–55]. Under this assumption, a two-gap model with energy gap parameters of 0.54 meV and 1.29 meV [56] was shown to reproduce well the temperature dependence of the measured specific heat [9]. However, it is noteworthy that in this case the energy value of the main gap is quite significantly larger than the latest reported results [10–13]. Moreover, Kačmarčík *et al.* [11] very detailed study of the specific heat capacity could not find any sign of a second energy gap. Further comparison of the two sets of data reveals that the jump in the specific heat near the critical temperature is much broader in Ref. [9] compared to Ref. [11], pointing towards highly homogeneous  $\text{Bi}_2\text{Pd}$  single crystals in the latter case. It is then likely that the observed hump belongs to other Bi–Pd superconducting alloys and the X-ray diffraction pattern indeed shows the presence of a  $\alpha$ - $\text{Bi}_2\text{Pd}$  phase [9].

Besides the temperature dependence of the specific heat, other measurements have been used to address the issue of multigap superconductivity. The temperature dependence of the lower critical field [10–12] and the magnetic field dependence of the superconducting gap [13] were very well described by one-gap models providing additional support for a standard single  $s$ -wave superconducting gap.

Finally, we calculate the quasi-particle density of states (DOS) in the superconducting state  $N_s(\omega)$  according to:

$$\frac{N_s(\omega)}{N_F} = \text{Re} \left[ \frac{\omega}{\sqrt{\omega^2 - \Delta^2(\omega)}} \right]. \quad (7)$$

Our results at 1 K are shown in Fig. 6 and compared directly to the experimental tunneling conductance of Ref. [10]. The superconducting DOS is scaled so that its high energy tail coincides with the DOS in the normal state. The agreement between our calculations and experiment is very good, all sets of data exhibiting two symmetric peaks characteristic of a single-gap structure.

## CONCLUSIONS

In conclusion, we have studied the superconducting properties of  $\beta$ - $\text{Bi}_2\text{Pd}$  within the *ab initio* anisotropic Migdal-Eliashberg theory. We have shown that the spin-orbit coupling only results in a slight increase in the predicted superconducting gap and critical temperature, while the structure of the superconducting gap remains practically unaffected. We find a sizable anisotropy in

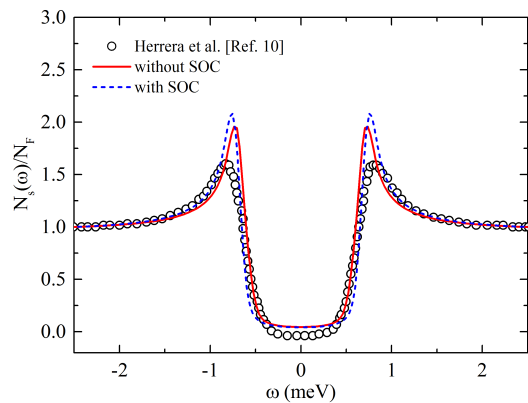


FIG. 6: (Color online) Calculated normalized quasi-particle DOS in the superconducting state of  $\text{Bi}_2\text{Pd}$  without (red line) and with (blue dashed line) SOC compared to tunneling data from Ref. [10] (black circles) for  $T = 1$  K.

the electron-phonon coupling leading to a single superconducting gap which varies in magnitude over the disconnected sheets of the Fermi surface. The experimental superconducting gap, critical temperature, specific heat, and tunneling conductance are well described assuming a conventional phonon-mediated mechanism as the origin of the superconducting transition.

## ACKNOWLEDGMENTS

We gratefully acknowledge fruitful discussions with A. Codlea and Z. Pribulová. J-J Zheng acknowledges the support from the China Scholarship Council (Grant No. 201508140043).

---

\* Corresponding author. E-mail address: rmargine@binghamton.edu (E.R. Margine).

- [1] N. N. Zhuravlev, Zh. Eksp. Teor. Fiz. **32**, 1305 (1957).
- [2] N. N. Zhuravlev, Sov. Phys. Crystallogr. **3**, 506 (1958).
- [3] B. T. Matthias, T. H. Geballe, and V. B. Compton, Rev. Mod. Phys. **35**, 1 (1963).
- [4] H. Okamoto, J. Phase Equilib. **15**, 191 (1994).
- [5] L. Jiao, J. L. Zhang, Y. Chen, Z. F. Weng, Y. M. Shao, J. Y. Feng, X. Lu, B. Joshi, A. Thamizhavel, S. Ramakrishnan, and H. Q. Yuan, Phys. Rev. B **89**, 060507(R) (2014).
- [6] M. Neupane, N. Alidoust, S.-Y. Xu, I. Belopolski, D. S. Sanchez, T.-R. Chang, H.-T. Jeng, H. Lin, A. Bansil, D. Kaczorowski, M. Z. Hasan, and T. Durakiewicz, arXiv:1505.03466v1 (2015).
- [7] Z. Sun, M. Enayat, A. Maldonado, C. Lithgow, E. Yelland, D. C. Peets, A. Yaresko, A. P. Schnyder, and P. Wahl, Nat. Commun. **6**, 6633 (2015).
- [8] D. C. Peets, A. Maldonado, M. Enayat, Z. Sun, P. Wahl, and A. P. Schnyder, Phys. Rev. B **93**, 174504 (2016).

- [9] Y. Imai, F. Nabeshima, T. Yoshinaka, K. Miyatani, R. Kondo, S. Komiyama, I. Tsukada, and A. Maeda, *J. Phys. Soc. Jpn.* **81**, 113708 (2012).
- [10] E. Herrera, I. Guillaumon, J. A. Galvis, A. Correa, A. Fente, R. F. Luccas, F. J. Mompean, M. García-Hernández, S. Vieira, J. P. Brison, and H. Suderow, *Phys. Rev. B* **92**, 054507 (2015).
- [11] J. Kačmarčík, Z. Pribulová, T. Samuely, P. Szabó, V. Cambel, J. Šoltýs, E. Herrera, H. Suderow, A. Correa-Orellana, D. Prabhakaran, and P. Samuely, *Phys. Rev. B* **93**, 144502 (2016).
- [12] P. K. Biswas, D. G. Mazzone, R. Sibille, E. Pomjakushina, K. Conder, H. Luetkens, C. Baines, J. L. Gavilano, M. Kenzelmann, A. Amato, and E. Morenzoni, *Phys. Rev. B* **93**, 220504 (2016).
- [13] L. Che, T. Le, C. Q. Xu, X. Z. Xing, Z. Shi, X. Xu, and X. Lu, *Phys. Rev. B* **94**, 024519 (2016).
- [14] Y.-F. Lv, W.-L. Wang, Y.-M. Zhang, H. Ding, W. Li, L. Wang, K. He, C.-L. Song, X.-C. Ma, and Q.-K. Xue, *arXiv:1607.07551v1* (2016).
- [15] M. Sakano, K. Okawa, M. Kanou, H. Sanjo, T. Okuda, T. Sasagawa, and K. Ishizaka, *Nat. Commun.* **6**, 8595 (2015).
- [16] I. R. Shein and A. L. Ivanovskii, *J Supercond Nov Magn* **26**, 1 (2013).
- [17] K. Zhao, B. Lv, Y. Y. Xue, X. Y. Zhu, L. Z. Deng, Z. Wu, and C. W. Chu, *Phys. Rev. B* **92**, 174404 (2015).
- [18] N. Marzari, A. A. Mostofi, J. R. Yates, I. Souza, and D. Vanderbilt, *Rev. Mod. Phys.* **84**, 1419 (2012).
- [19] F. Giustino, M. L. Cohen, and S. G. Louie, *Phys. Rev. B* **76**, 165108 (2007).
- [20] F. Giustino, *arXiv:1603.06965v1* (2016).
- [21] J. P. Perdew, *Phys. Rev. Lett.* **55**, 1665 (1985).
- [22] N. Troullier and J. L. Martins, *Phys. Rev. B* **43**, 1993 (1991).
- [23] M. Fuchs and M. Scheffler, *Comput. Phys. Commun.* **119**, 67 (1999).
- [24] P. Giannozzi *et al.*, *J. Phys. Condens. Matter* **21**, 395502 (2009).
- [25] J. P. Perdew, K. Burke, and M. Ernzerhof, *Phys. Rev. Lett.* **77**, 3865 (1996).
- [26] In agreement with Ref. [16], we find that the optimized lattice parameters with and without the inclusion of SOC are very closed to each other and less than 2% larger than the experimental values. This slight increase in the lattice constants will only have a minor effect on the magnitude of the superconducting gap and critical temperature, without affecting the overall conclusions.
- [27] A. Y. Liu, I. I. Mazin, and J. Kortus, *Phys. Rev. Lett.* **87**, 087005 (2001).
- [28] M. D. Johannes, I. I. Mazin, and C. A. Howells, *Phys. Rev. B* **73**, 205102 (2006).
- [29] R. Bianco, M. Calandra, and F. Mauri, *Phys. Rev. B* **92**, 094107 (2015).
- [30] T. Chang *et al.*, *Phys. Rev. B* **93**, 245130 (2016).
- [31] S. Baroni, S. de Gironcoli, A. Dal Corso, and P. Giannozzi, *Rev. Mod. Phys.* **73**, 515 (2001).
- [32] P. B. Allen and B. Mitrović, *Solid State Phys.* **37**, 1 (1982).
- [33] E. R. Margine and F. Giustino, *Phys. Rev. B* **87**, 024505 (2013).
- [34] J. Noffsinger, F. Giustino, B. D. Malone, C.-H. Park, S. G. Louie, and M. L. Cohen, *Comput. Phys. Commun.* **181**, 2140 (2010).
- [35] S. Poncé, E. R. Margine, C. Verdi, and F. Giustino, *Comput. Phys. Commun.* **209**, 116 (2016).
- [36] E. R. Margine and F. Giustino, *Phys. Rev. B* **90**, 014518 (2014).
- [37] E. R. Margine, H. Lambert, and F. Giustino, *Sci. Rep.* **6**, 21414 (2016).
- [38] J.-J. Zheng and E. R. Margine, *Phys. Rev. B* **94**, 064509 (2016).
- [39] C. Heil, S. Poncé, H. Lambert, E. R. Margine, and F. Giustino, *Phys. Rev. Lett.* (under review).
- [40] A. A. Mostofi, J. R. Yates, Y.-S. Lee, I. Souza, D. Vanderbilt, and N. Marzari, *Comput. Phys. Comm.* **178**, 685 (2008).
- [41] For a wide range of superconductors, a value of  $\mu^*$  in the range 0.1–0.2 has been found, but in several cases values outside of this range are necessary to explain experimental critical temperatures [37, 39, 42, 43].
- [42] J. Bauer, J. E. Han, and O. Gunnarsson, *J. Phys.: Condens. Matter* **24**, 492202 (2012).
- [43] A. Subedi, L. Ortenzi, and L. Boeri, *Phys. Rev. B* **87**, 144504 (2013).
- [44] H. J. Vidberg and J. W. Serene, *J. Low Temp. Phys.* **29**, 179 (1977).
- [45] C. R. Leavens and D. S. Ritchie, *Solid State Commun.* **53**, 137 (1985).
- [46] W. Setyawan, and S. Curtarolo, *Comput. Mater. Sci.* **49**, 299 (2010).
- [47] See Supplemental Material at [URL] for Supplemental Figures S1-S6.
- [48] The superconducting gap was extracted using the data in Ref. [11], namely  $2\Delta/k_B T_c = 4.1$  and  $T_c = 5$  K.
- [49] The superconducting gap was extracted using the data in Ref. [11], namely  $2\Delta/k_B T_c = 3.7 \pm 0.1$  and  $T_c = 5$  K.
- [50] J. Bardeen, L. N. Cooper, and J. R. Schrieffer, *Phys. Rev.* **108**, 1175 (1957).
- [51] H. Padamsee, J. E. Neighbor, and C. A. Shiffman, *J. Low Temp. Phys.* **12**, 387 (1973).
- [52] D. C. Johnston, *Supercond. Sci. Technol.* **26**, 115011 (2013).
- [53] F. Bouquet, R.A. Fisher, N.E. Phillips, D.G. Hinks, and J.D. Jorgensen, *Phys. Rev. Lett.* **87**, 047001 (2001).
- [54] H. D. Yang, J.-Y. Lin, H. H. Li, F. H. Hsu, C. J. Liu, S.-C. Li, R.-C. Yu, and C.-Q. Jin, *Phys. Rev. Lett.* **87**, 167003 (2001).
- [55] Y. Wang, T. Plackowski, and A. Junod, *Physica C* **355**, 179 (2001).
- [56] The two energy gap parameters were extracted using the data in Ref. [9], namely  $2\Delta_1/k_B T_c = 2.5$ ,  $2\Delta_2/k_B T_c = 6$ , and  $T_c = 5$  K.